PLANETARY GEOLOGY: IMPACT PROCESSES ON ASTEROIDS

Final Report for Contract NASW-3208

P.I.: Clark R. Chapman
Co. I.: Donald R. Davis
Richard Greenberg
Stuart J. Weidenschilling

I. Introduction

Our goal is to understand the fundamental geological and geophysical properties of asteroids by theoretical and simulation studies of their collisional evolution. We have developed numerical simulations incorporating realistic physical models to study the collisional evolution of hypothetical asteroid populations over the age of the solar system. Our ideas and models are constrained by the observed distributions of sizes, shapes, and spin rates in the asteroid belt, by properties of Hirayama families, and by experimental studies of cratering and collisional phenomena. Our studies to date suggest that many asteroids are gravitationally-bound "rubble piles." Those that rotate rapidly may have non-spherical quasi-equilibrium shapes, such as ellipsoids or binaries. Through comparison of our models with astronomical data, we may be able to determine physical properties of these asteroids (including bulk density) and shed light on physical processes that have operated in the solar system in primordial and subsequent epochs.

During the past year, we have made extensive improvements in our numerical models for studying the collisional evolution of asteroid spins and asteroid sizes. In Section II, we describe the collisional outcome algorithm that forms the basis for our collisional evolution scenarios. In Section III, we outline the numerical evolution models used to study the collisional evolution of asteroid sizes and spins, together with some tests of the collisional algorithm including comparison of collisional outcome models with observed Hirayama families. In Section IV, the collisional evolution of asteroid sizes

and spins is discussed, while Section V gives an overview of future directions in this project.

II. Collisional Outcome Model

The general framework of our collisional outcome model is described by Greenberg et al. (1978) and Davis et al. (1979). Briefly, the outcome of a collision (catastrophic disruption, cratering, inelastic rebound) between two bodies is modeled as a function primarily of the collisional energy relative to the inherent strength and size of the colliding bodies. Since we are studying the collisional evolution of asteroids whose orbits are eccentric and inclined enough to give a mean impact speed of 5 km/s, disruption and cratering are the only collisional outcomes that are relevant; the categories of simple rebound and rebound with cratering, defined by Greenberg et al. are never encountered for plausible material properties at asteroidal impact speeds.

A. Size Distribution of Collisional Fragments:

A collision between a larger (target) body of mass, m_t, and a smaller (projectile) body, m_p, at a speed, v, generates a collisional energy, E, in the center-of-mass frame where

$$E = \frac{m_p m_t v^2}{2(m_p + m_t)} \qquad (1)$$

What is the outcome of such a collision? This depends on the "impact strengths" of the bodies, where the impact strength is defined as the collisional energy per unit volume delivered to a body that produces a largest fragment that contains 1/2 of the original bodies' mass. Experimental studies by Gault and Wedekind (1969), Fujiwara et al. (1977), and Hartmann (1978) show that there is a large change in the mass fraction contained in the largest fragment over

a narrow range of collisional energy densities. The energy density at which the sharp transition from cratering to catastrophic shattering occurs varies with the type of material: For basalts and strong rocky material, it occurs at ~3×10^7 ergs/cm^3; for water ice, at about ~2×10^5 ergs/cm^3; for loosely-bound dirt clouds, ~10^4 ergs/cm^3; for iron, ~10^9 ergs/cm^3. We emphasize, however, that the impact strength is used parametrically to describe the results of actual impact experiments, and care must be used in inferring other material properties from an impact strength alone.

Experimental results concerning the size of the largest fragment from a collision are represented by a least-square data fit:

$$\frac{m_\ell}{m_t} = 0.5\left(\frac{Sm_t}{\rho E}\right)^{1.24} \qquad (2)$$

where m_ℓ is the mass of the largest fragment, ρ is the target density, and S is the impact strength of the target. If the collisional energy per unit volume just equals the impact strength, then the largest fragment contains 1/2 of the original mass and the body is said to just be shattered. Collision energy densities less than S produce cratering outcomes, as described on p. 6 below. How big a projectile is needed to just barely shatter a given body? The size ratio between projectile and target depends on the impact speed and the impact strength. Experiments by Hartmann (1980) indicate that for comparable impact strengths between the target and projectile the collisional energy is divided equally between the two bodies. We may then solve for the target/projectile size ratio to just shatter the target body, γ, from eq. (1):

$$\gamma = \left\{\frac{\rho_p}{\rho_t}\left(\frac{\rho_t v^2}{2S} - 1\right)\right\}^{1/3} \qquad (3)$$

A power-law model is adopted to describe the fragmental population size distribution (Greenberg et al., described here). The slope of the distribution

is determined by the total mass of fragments, given the largest fragment mass (see above).

B. Velocity Distribution of Collisional Fragments:

A cumulative power law velocity distribution for the fragments is of the form

$$f = (v/v_k)^{-\alpha} \quad \text{if } v \geq v_k$$
$$f = 1 \quad \text{if } v < v_k \qquad (4)$$

where f is the ejecta mass fraction moving faster than v, v_k is the minimum ejecta speed, and α is a model parameter. Gault et al. (1963) gave $\alpha = 9/4$ for cratering into basalt, and Greenberg et al. adopt the same slope for cratering impacts into sand, as implied by experiments of Stöffler et al. (1975). For shattering impacts, Greenberg et al. use a constant fragment velocity which is equivalent to a large value of α.

For a collision which produces an ejecta mass m_e, the amount of collisional energy that is partitioned into ejecta kinetic energy, f_{ke}, is used to calculate v_k. For a given impact, 1/2 the available collisional energy is nominally assumed to go into each body, an assumption which is supported by experiments for bodies of comparable impact strengths. Further data are needed to determine the energy partitioning when the projectile and target strengths differ significantly (Hartmann, 1980). The parameter v_k is found from the total energy partitioned into ejecta energy. The total kinetic energy carried by the ejecta is found by integrating the mass-velocity distribution (eq. 4), over all velocities from v_k to some upper bound, v_{max}. If $\alpha > 2$ and $v_{max} >> v_k$, then the total ejecta kinetic energy is a function of v_k and can be equated to $f_{ke} \cdot E/2$. Solving this relation for v_k yields,

$$v_k = \left[\frac{E \cdot f_{ke}}{m_e} \quad \frac{\alpha - 2}{\alpha}\right]^{1/2} \qquad (5)$$

Fujiwara and Tsukamoto (1980) measured fragment speeds from catastrophic disruption of basalt targets. They found that the fragments do have a distribution of speeds and that 70 - 80% of the ejecta mass moves slower than $6.4 \times 10^{-5} (E/M)^{0.76}$ cm/s, where E/M is the collisional energy per gram of target. Their measurements excluded the 20% or so of mass closest to the impact site, which presumably contains the highest speed ejecta. Typically only a few percent of the collisional kinetic energy, or less, appeared as ejecta kinetic energy. The ejecta speed algorithm in eq. (4) is in fair agreement with the experimental results if the same fraction of collisional energy is partitioned into ejecta kinetic energy in the model as was experimentally determined. The nominal collisional model adopted by Davis et al. (1979) partitions 10% of the collisional energy for each body into ejecta kinetic energy (i.e., 5% of the total collisional energy goes into ejecta for each of the projectile and target). With the 9/4 exponent for the velocity distribution, most of the ejecta KE is carried by the high speed tail; indeed, only 16% of the ejecta KE is carried by the slowest moving 80% of the ejecta. Hence, the nominal 0.1 energy partitioning parameter of Davis et al. translates into about 1% for comparison with the measured values of Fujiwara and Tsukamoto. They find ejection energy fractions from 0.3 - 3.5%, so the 1% partitioned using our nominal parameters is right in the middle of the experimental range.

C. Formation of Gravitationally-Bound Rubble Piles:

If the body is completely shattered and the minimum ejecta speed v_k is larger than the escape speed v_e of the body, then the fragments are totally dispersed; otherwise, only the fraction of ejecta given by (4) with $v = v_e$ escapes the body. The remaining ejecta are gravitationally recaptured. Such a process in which the body is shattered but only a small fraction escapes the gravity field leads to the formation of gravitationally-bound "rubble piles."

If a fraction, f, of the ejecta escapes, what is the size distribution of the escaping fragments? We assume that the gravitationally-bound fraction, (1 - f), includes the largest fragment from the collision. The largest escaping fragment is taken to be a fraction f, as found from (4), of the largest fragment mass calculated from (2). Also, the mean speed of the ejecta after escaping the gravity field of the asteroid is found from

$$\overline{V_{ej}^2} = V_k^2 \alpha/(\alpha - 2) - V_e^2 \qquad (6)$$

This method is used to determine (a) the outcome of shattering collisions, in which the collisional energy in the center-of-mass frame is large enough to shatter the body, and (b) the size and velocity distribution of the fragments.

D. Cratering Collisions:

If the body is not shattered, it is then said to be cratered. The cratering algorithm is described by Greenberg et al. and has been modified only to include oblique impacts as described below. The model retains the energy scaling relation for calculating the total amount of ejecta produced by a given impact. This algorithm introduces a discontinuity in the size of the largest fragment at the boundary between cratering and shattering events. Whereas an impact that just shatters the body produces a largest fragment containing 50% of the initial target mass, an impact just slightly less energetic produces a largest fragment many orders of magnitude less massive: for $S = 3 \times 10^7$ ergs/cm^3, the largest fragment is 10^9 times less massive for cratering than for shattering. Several approaches are being considered to eliminate this large discontinuity.

The collisional outcome model described above is for head-on impacts. However, real asteroid collisions occur at all impact angles, from central collisions to grazing impacts. Impact experiments by Fujiwara et al. (1980) and Gault (1973) indicate that collisional outcomes depend on the impact angle

as well as collisional energy and material properties. To account for oblique impacts, we have modified the collisional outcome model so that the fragmental size distribution and energy partitioning depend on impact angle. We then use the probability distribution for impact angles onto spherical targets to average over all impact angles in order to find the mean values for the largest fragment and energy partitioning coefficient.

The geometry for calculating the distribution of impact angles is shown in Figure 1.

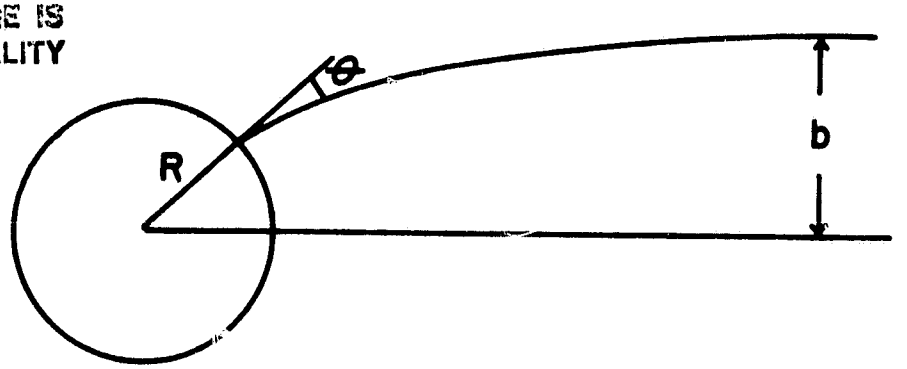

Figure 1: Trajectory geometry for calculating the probability distribution of impact angles.

Particles approaching the target body on trajectories that are offset a distance, b, from the center of the target body are gravitationally attracted by the target and impact at an angle θ from the local vertical. The impact angle, θ, and the impact parameter, b, are related by

$$\sin\theta = \frac{b}{R} \cdot \frac{1}{\sqrt{1 + (V_e/V_\infty)^2}} , \qquad (7)$$

where V_e is the escape speed from the surface of the body, and V_∞ is the approach speed far from the target.

Assuming a uniform distribution of impact parameters in the plane perpendicular to the approach asymptote, the probability of approaching with an impact

parameter between b and b + db is:

$$dP(b) \propto 2\pi\, b\, db \tag{8}$$

Using eq. (7) to replace b with θ and then normalizing over all impact parameters, we find the probability distribution for impacting with an angle between θ and $\theta + d\theta$ to be:

$$P(\theta)d = 2 \sin\theta \cos\theta\, d\theta;\ 0 \leq 0 \leq 90^{0}. \tag{9}$$

Impact experiments by Fujiwara et al. (1981) indicate that the oblique impacts are less efficient than head-on impacts in shattering a target. In particular, comminution decreases, hence the largest fragment size increases, with increasing impact angle:

$$f_{\ell}(\theta) = \frac{f_{\ell}(0)}{\cos^{3}\theta} \quad \text{for } 0 < \theta < \theta_{m} \text{ and}$$
$$f_{\ell} = 1 \quad \text{if} \quad \theta > \theta_{m}, \tag{10}$$

where $f_{\ell}(\theta) = m_{\ell}(\theta)m_{t}$, $f_{\ell}(0)$ is the fractional mass of the largest fragment for head-on impacts, and θ_{m} is the value of θ for which $f_{\ell} = 1$. The mean value of $f_{\ell}(\theta)$ is found from

$$\overline{f_{\ell}} = \int_{0}^{\theta_{m}} f_{\ell}(\theta)\, P(\theta)\, d\theta, \tag{11}$$

which yields using $P(\theta)\, d\theta$ from eq. (9):

$$\overline{f_{\ell}} = \frac{2\, f_{\ell}(0)^{2/3}}{1 + f_{\ell}(0)^{1/3}} \tag{12}$$

Table 1 compares the mean size of the largest fragment averaged over all impact angles with that for head-on impacts. The inclusion of oblique impacts produces larger fragments, ranging from ~40% larger for what would be a barely

TABLE 1: FRACTIONAL MASS OF LARGEST FRAGMENT

$f_\ell(0)$ Central Impacts	$\overline{f}_\ell$ Mean For Oblique Impacts
0.50	0.70
0.1	0.29
0.01	0.08
0.001	0.018

TABLE 2: MEAN VALUE OF f_{ke} COMPARED WITH CENTRAL IMPACT VALUE

$f_{ke}(0)$	$\overline{f}_{ke}$
0.5	0.56
0.25	0.34
0.10	0.21
0.01	0.134

catastrophic impact in the head-on case to increases of more than an order of magnitude for very catastrophic impacts.

The energy partitioned into ejecta kinetic energy is assumed also to depend on the impact angle. The model described in Section IV (collisional evolution of spins) is adopted:

$$f_{ke}(\theta) = f_{ke}(0) + (1-f_{ke}(0)) \sin^6\theta, \tag{13}$$

where $f_k(0)$ is the energy partitioning coefficient for central impacts. Averaging over all impact angles yields the mean value $\overline{f}$ to be:

$$\overline{f}_{ke} = \frac{7f_{ke}(0) + 1}{8}$$

The mean value of f_{ke} is compared with the central impact value in Table 2. Adopting the mean value of f_{ke} implies that small values of energy partitioning are not allowed with 0.125 being the minimum value. In the absence of any experimental data in this area, we adopt this model, but remain cognizant of the limitation it might impose.

The previous discussion has addressed the effects of oblique impacts on catastrophic collisions, and we now address variations in cratering outcomes with impact angle. Experimental data by Gault et al. (1973) indicate that the amount of ejecta varies as $\cos^2\theta$, a result which we incorporate into the algorithm. As the mean value of $\cos^2\theta$ over all impact angles is 1/2, the ejecta mass is reduced by a factor of 2 from the value calculated for central impacts to account for oblique impacts.

III. Collisional Evolution Model

The basic structure of the collisional evolution program has been described by Chapman and Davis (1975) and Greenberg et al. (1978). Briefly, an arbitrary

population size distribution is modeled using a series of diameter bins with the bin width being a program parameter. Typically, each bin spans a factor of 2 in mass, and up to 30 diameter bins may be used to represent the population. The bins are used to represent the large size end of the population from the largest bodies down to some minimum diameter, D_{min}, determined by the largest body and the bin width. Particles smaller than D_{min} are represented by a power law, which is attached to the small end of the smallest diameter bin and has a slope equal to the mean slope of a power law size distribution fit to the smallest six diameter bins. The power law "tail" to the population is used to calculate collisional effects due to particles as small as 1 meter in size on larger bodies in the discrete diameter bins. Interactions among small particles in the tail are not considered. Also, only collisions with small tail particles energetic enough to shatter a body in a diameter bin are modeled; cratering impacts involving tail particles are excluded.

The collisional evolution of this system is calculated using a series of time steps, where the length of a time step is dynamically calculated so that no important physical parameter of the system can change by more than a fixed fraction. Typically a change no more than 50% during a single time step is allowed in the population of any diameter bin or in the mean eccentricity and inclination of the orbits for any bin. During each time step, the number of collisions that occur between the particles in two bins (the larger size bin, the target, and the smaller projectile) is calculated. The collisional outcome algorithm previously described is applied. Collisional fragments are distributed among the appropriate diameter bins, and the orbital changes due to collisions and gravitational close encounters are calculated. All pairs of diameter bins are treated, including interactions of particles in a bin with themselves. If there are more than ten collisions for a diameter-bin pair,

then the number of collisions is calculated deterministically using the particle-in-a-box algorithm for the number of collisions during the time step. If fewer than 10 collisions are predicted, then the actual number of collisions is calculated using a Poisson probability distribution and a random number generator. (However, the collision outcome is still calculated as described earlier.)

The collisional evolution model has recently been extended to treat the evolution of two interacting populations having different physical properties and moving on different orbits. The same collisional outcome algorithm as previously described is used with the physical parameters appropriate for each population. All interactions of each diameter bin with all other diameter bins in both populations is treated. Collision fragments are distributed into diameter bins for the population that the fragmented body belonded to; however, accretionary events involving particles from two different populations are placed in, and assumed to have the physical properties of, the population of the larger ("target") particle. (Time steps are calculated and the collisional evolution calculated as described previously.)

In addition to tracing the changes in the population size distribution and orbit distribution, we have begun recently to calculate the effect of collisions on the physical state of bodies of various sizes. Gravitationally-bound bodies are typically shattered many times before they are disrupted, so we keep track of the mean collisional energy that has been delivered to a given size body at any time during the collisional evolution. The number of surviving original bodies at any size is also calculated, along with the number that are eroded fragments or fragments from catastrophic disruptions at larger sizes.

Several checks were run comparing the predicted evolution using the two component simulation with that of the one component model (i.e., the single

component was input to one of the population distributions, while the other population was set to zero, or the single component was divided equally between the two populations). The evolution was the same in all of the test cases.

We also compared the numerically calculated evolution with the analytic models of Dohnanyi (1971), after first changing the collisional physics to agree with that of Dohnanyi. Principally, this required elimination of gravitational binding since Dohnanyi did not explicitly include this factor in his models. In most cases, reasonably good agreement was found between the numerical and the analytic theories.

Our collisional algorithms are applied to predict the outcome of impacts involving large bodies (i.e., ~10 - ~10^3 km in size). Yet these algorithms are based upon experimental results involving laboratory-scale targets, hence we assume that scaling laws are valid over many orders of magnitude in mass. The best test of the validity of our collisional outcome models would be to compare our calculated results with the observed properties of Hirayama families, widely thought to be the remnants of major asteroid collisions. Colorimetric studies by Gradie and Tedesco (Gradie et al., 1979) find spectral similarities among members of several large families, while many of the smaller families exhibit diversity, implying that they may be the fragments of a single differentiated parent body. Hirayama families provide us with natural experiments with which to compare our numerical collisional outcome algorithms.

We selected the Themis and the Eos families for study. These are large, well-defined families having many members that are spectrally similar. Also, minimum diameter reconstructions of the parent asteroid have been carried out by Gradie. To compare our predicted collisional outcome with the observed family distribution, we must first determine the type of collision with the parent body that produced the fragments. (We suppose that there has been little

subsequent collisional evolution of the fragments.) If the largest member of the family contains less than 50 - 60% of the parent body's mass, we classify the impact as one that shattered the target body. We then calculate the collisional energy necessary to produce the observed largest fragment, and then calculate the size distribution of the fragments along with their mean v_∞ relative to the parent asteroid. The calculated distribution and v_∞ are then compared with observed quantities.

A. Themis Family:

This is a populous, well-defined family whose parent body was a large C-type asteroid at least ~300 km in diameter (Gradie et al., 1979). Sizes and types of the largest family members are given in Table 3 and are shown to scale in Figure 2. If we assume that the parent asteroid had a diameter of 300 km, then the largest fragment (24 Themis) contains about 60% of the target's mass. If we adopt the nominal impact parameters for C asteroids described by Davis et al. (1979, see Table 4) and calculate the outcome for a collision that delivers just enough energy to barely shatter the body and produce a fragment the size of 24 Themis, we find that there is not nearly enough ejecta KE to disperse the fragments against the parent-Themis gravity field. Hence, the outcome is dominated by a fractured parent body that is nearly as big as it was before the collision. To produce a body as small as Themis requires a considerably more energetic collision. In fact, the minimum collisional energy to produce Themis can be calculated using collisional parameters that enhance disruptive outcomes (i.e., increase f_{ke} to 50%, obviously it can't be more than or even equal to 100%, and 50% is probably a reasonable upper bound for the fraction into ejecta KE), and increase the slope of the ejecta velocity distribution to a large number (~10 or so). Physically, the changes correspond to having all of the ejecta launched at nearly the same speed (barely more than

TABLE 3: SIZE AND TYPE OF THE LARGEST ASTEROIDS IN SEVERAL HIRAYAMA FAMILIES

Family	Asteroid	Diameter (km)	Spectral Type
1. Themis	24	249	C
	90	138	C
	222	85	C
	268	85	U
	171	80	U
2. Eos	221	98	U
	579	80	S
	639	68	S
	966	62	C
	798	61	SM

TABLE 4: COLLISIONAL EVOLUTION PROGRAM PARAMETERS

	C Asteroids	S Asteroids
Density (g cm^{-3}), ρ	2.5	3.5
Impact strength (erg cm^{-3}), S	6×10^4	3×10^7
Mean collision speed (km sec^{-1})	5	5
Fraction of KE into ejecta KE, f_{ke}	0.1	0.1
Slope of ejecta velocity distribution, α	2.25	2.25
Mass excavation coefficient for cratering impacts, grams per erg of collisional energy	10^{-8}	10^{-9}

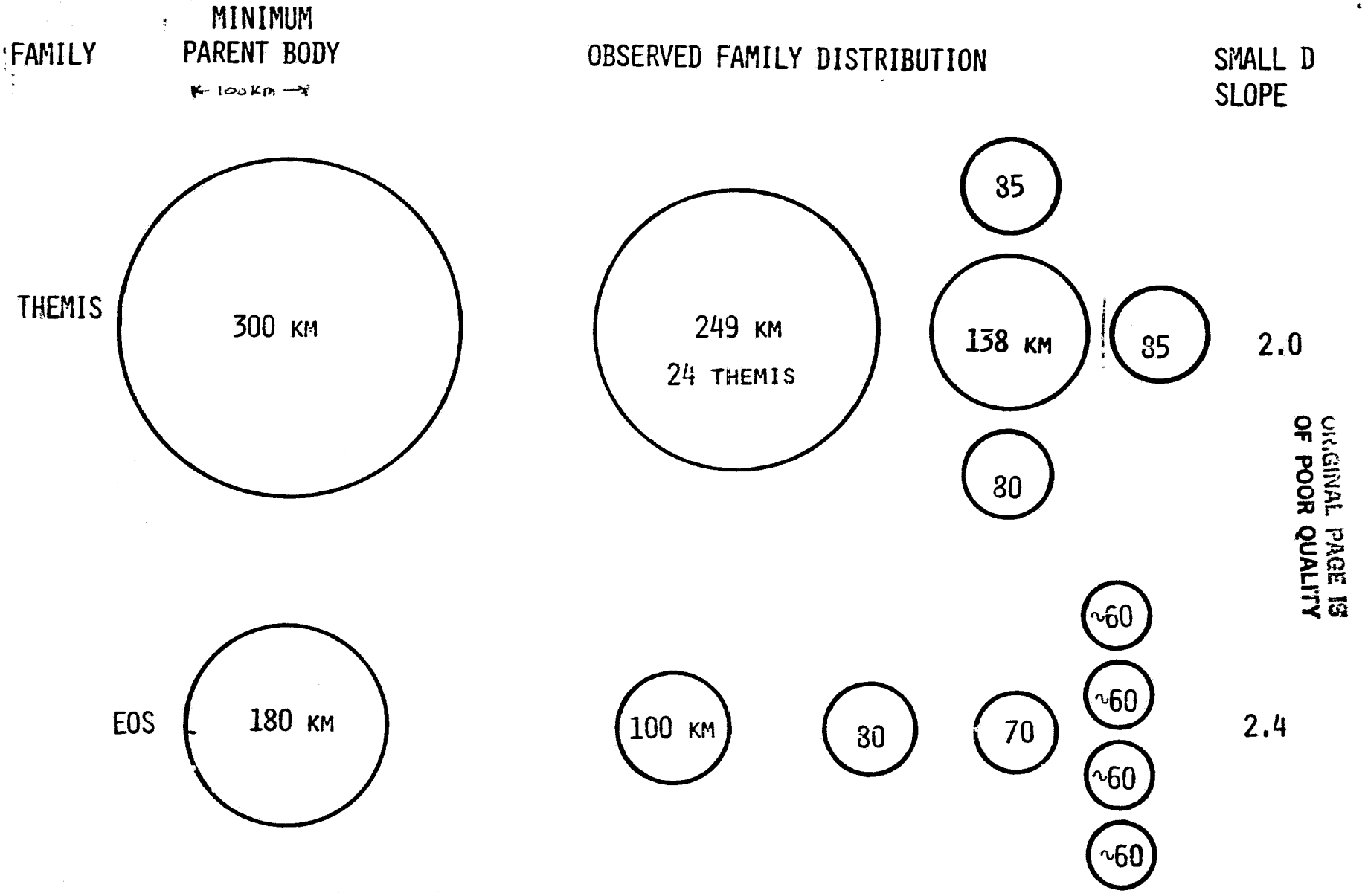

FIGURE 2: Observed size distribution for the Themis and Eos families, to scale of 1 cm = 50 km.

escape velocity) which minimizes the total ejecta KE required to disrupt the asteroid. With these changes to the collisional parameters, we now find that a collision delivering 2×10^{31} ergs will shatter and disperse the 300 km diameter target and produce a largest body ~250 km diameter (i.e., 24 Themis). But the second largest fragment is found to be only ~15 km in size, whereas the observed second largest fragment has a diameter of 138 km. In our models, all bodies from the second largest down in size are assumed to be collisional fragments -- only the largest body may be a gravitationally-bound rubble pile. The only way to increase the size of the smaller fragments in the collisional model is to increase the impact strength. In fact, if an impact strength of 5×10^{8} ergs/cm^3 is adopted for C asteroids (an increase of 5×10^{4}!!), then the predicted collisional outcome is in reasonably good agreement with the observed Themis family, as shown in Figure 3.

B. Eos Family:

This family is another well-defined, populous family, but its members are dominantly S asteroids. Table 3 lists the largest family members. Gradie (1978) estimated the minimum parent body size to be 180 km; if so, then the collision was quite catastrophic. Following the same procedure as for the Themis family, we find that a collision that produces a largest shattered fragment containing ~16% of the initial mass does not accelerate the ejecta enough to overcome gravitational binding. The fragments mostly fall back together, and the reassembled body contains over 99% of the initial mass. Even the more efficient parameters for dispersal against gravity ($f_{ke} = 0.5$, described earlier) produce a largest fragment that has 98% of the initial mass. As was the case for the Themis family, the only way to disperse a significant fraction of the initial mass is with much more energetic collision. But more

"CHIPS-OFF-THE-BLOCK" MODEL

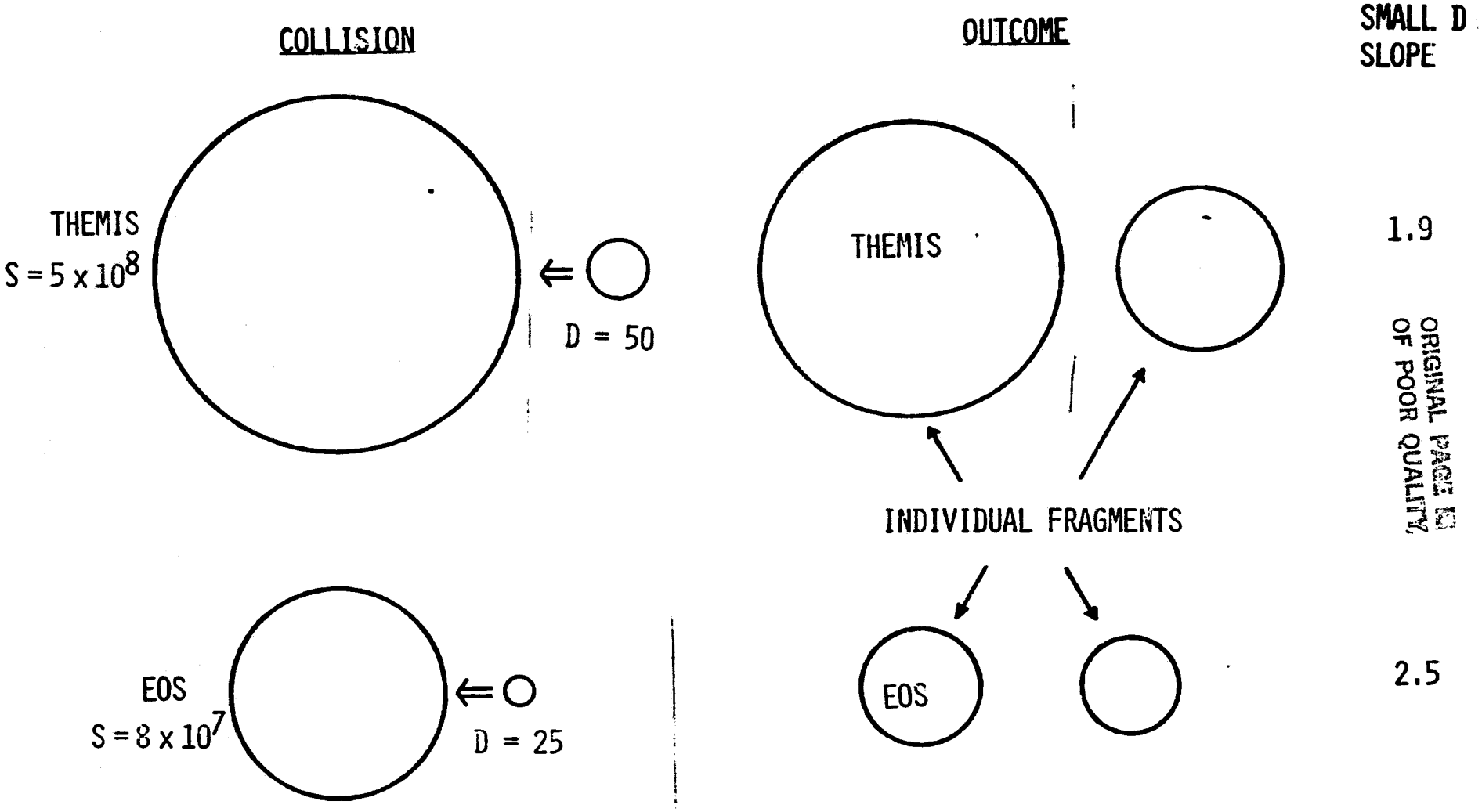

FIGURE 3: Predicted collisional outcome for Themis and Eos families, with very strong impact strengths. Same scale as Figure 2.

energetic collisions thoroughly smash the original, and the second and third largest fragments are again too small, unless the impact strength is again increased. The best "fit" to the Eos family requires an impact strength $S = 8 \times 10^7$ ergs/cm^3, $f_{ke} = 0.50$, and nearly constant velocity. Figures 2 and 3 compare the observed and predicted size distribution for this family.

Both the predicted Themis and Eos families fail to match the observed family distribution using the nominal asteroid collision parameters: In both cases, the observed population has the second, third, etc. largest asteroid much larger than calculated when the largest fragment is forced to agree with the observed largest family member. Hence, either our nominal parameters are incorrect, or our physical models are not appropriate for the case we are trying to model.

Two solutions to this dilemma have been discussed recently. Fujiwara (1982) and Chapman et al. (1982) suggest that gravitational reaccumulation takes place among the ejecta fragments; hence, not only the largest body, but also many other large bodies among the collisional products may be gravitationally-bound rubble piles. In this case, the large-size distribution is not controlled by the fragmental distribution resulting from the collision, but rather by the dynamics of the gravitational reaccumulation process -- a process which has not yet been studied quantitatively. Further progress in understanding the effectiveness of gravitational reaccumulation of collisional ejecta awaits a better understanding of the mass-velocity relation for catastrophic collisions.

Another hypothesis suggested by Davis et al. (1982) is that the impact strength of large bodies increases with the size of the body due to internal self-compression. If the basic fracturing mechanism for impacts is tensional failure of material during passage of a rarefaction wave produced by the reflection of an elastic compressive wave at a free surface, then the strength

of the rarefaction wave must be sufficiently great to overcome both the intrinsic tensile strength of the material plus the loading due to internal self-compression of the body. Assuming that the experimentally determined impact strength is a measure of the rarefaction wave strength required to exceed the dynamic tensile strength of the material, then one needs to add the internal pressure to the intrinsic impact strength in order to find the effective impact strength for large bodies. To calculate the impact strength as a function of target size, we add the compressive pressure at a depth below which half the mass of the body lies to the intrinsic impact strength, S_0:

$$S(D) = S_0 + P, \tag{14}$$

where $P = 0.37P_c \simeq \frac{\pi G \rho^2 D^2}{16}$ with P_c being the central pressure of the body. For this calculation, the body is assumed to be spherical with constant density. P is the pressure at a depth of 21% of the radius of the body, where 50% of the mass is below this depth.

How does the impact strength vary with size in the model? For small bodies, the impact strength is constant, equal to the intrinsic impact strength; while for large bodies, the impact strength is determined by the pressure term. For a basalt body with a density of 3.0 gm/cm^3 and a nominal impact strength of 3×10^7 ergs/cm^3, the effective impact strength is double the nominal value in a body 160 km in diameter. Bodies larger than 250 - 300 km have impact strengths dominated by internal compression if they are made of basalt-like or weaker materials.

The above described model certainly works in the direction to bring the calculated collisional outcomes for Hirayama families into better agreement with the observed values. Using the above model, the effective impact strength for the parent Themis body is 7×10^7 ergs/cm^3, while that for parent Eos is 8×10^7 ergs/cm^3. This is very close to the required impact strength to pro-

duct the observed Eos family by our model, but the strength is about a factor of 8 too small for the Themis family. Clearly more work is required to better understand the above model for scaling impact strength, but such an approach is qualitatively in the right direction and of the right magnitude for one of the families considered.

IV. Studies of Asteroid Collisional Evolution

A. Size Evolution:

We have applied the numerical collision evolution model to study the evolution of a variety of hypothetical initial asteroid populations over the 4.5 b.y. age of the solar system. We wish to learn about which initial populations could collisionally evolve to the present asteroid belt, assuming the dynamical environment of the asteroids has been constant over most of solar system history. The assumption of dynamical "uniformitarianism" cannot hold back to the accretional stage of asteroid history, since accretion cannot occur for any reasonable geologic material at impact speeds of ~5 km/s. Really, we are studying the collisional evolution of asteroids subsequent to the time when asteroid orbits were stirred up, resulting in the large mean impact speed of ~5 km/s. We seek to answer questions such as: What was the mass of the asteroid belt when their orbits were randomized? What initial size distributions are consistent with the present belt? How do physical and geological parameters affect the collisional evolution?

The total mass in the asteroid zone must have been much larger, assuming the belt formed largely as a result of accretion in its current location, otherwise the accretion time for large asteroids exceeds the age of the solar system. Was there a mass of 1 - 2 $M_\oplus$ in the asteroids at the time their orbits were randomized and is collisional evolution an efficient enough process to grind down and remove most of this initial mass from the asteroid zone? Or

did mass depletion have to occur prior to, or as part of, the processes that established the current dynamical environment?

We are interested also in studying the physical state of asteroids resulting from the collisional environment in the belt, as well as calculating the number of original asteroids that might exist at various sizes. Several algorithms have been added to the collisional model in order to keep track of the average collisional energy delivered to asteroids prior to their disruption, the total number of bodies added to and removed from each size bin, the number of original bodies that survive to the end of the simulation, and the number of asteroids created by cratering erosion and gravitationally-bound cores. Figure 4 illustrates the flow of asteroids through a typical size bin.

Collisional evolution over 4.5 b.y. for several hypothetical initial populations is shown in Figures 5, 6, and 7. The effect of initial population mass on the final population for initial power law size distributions containing 0.1 $M_\odot$ and 0.01 $M_\odot$ is shown in Fig. 5. Both initial populations evolve to the present belt for sizes smaller than ~100 km diameter, but larger asteroids are overabundant relative to the present belt. Increasing the kinetic energy partitioned into ejecta energy makes it easier to disrupt large asteroids as shown in Fig. 6. The evolution of several minimum mass initial populations is illustrated in Fig. 7. Variations in the evolution due to changing the impact strength are shown for three cases: (i) constant, weak strength of 10^4 ergs/cm^3, (ii) constant, strong strength of 10^8 ergs/cm^3, and (iii) the size-dependent impact strength model involving internal pressure, as previously described. While none of these cases evolves to the present belt, the variable strength case is the best match, while case (ii) gives the poorest fit to the observed belt.

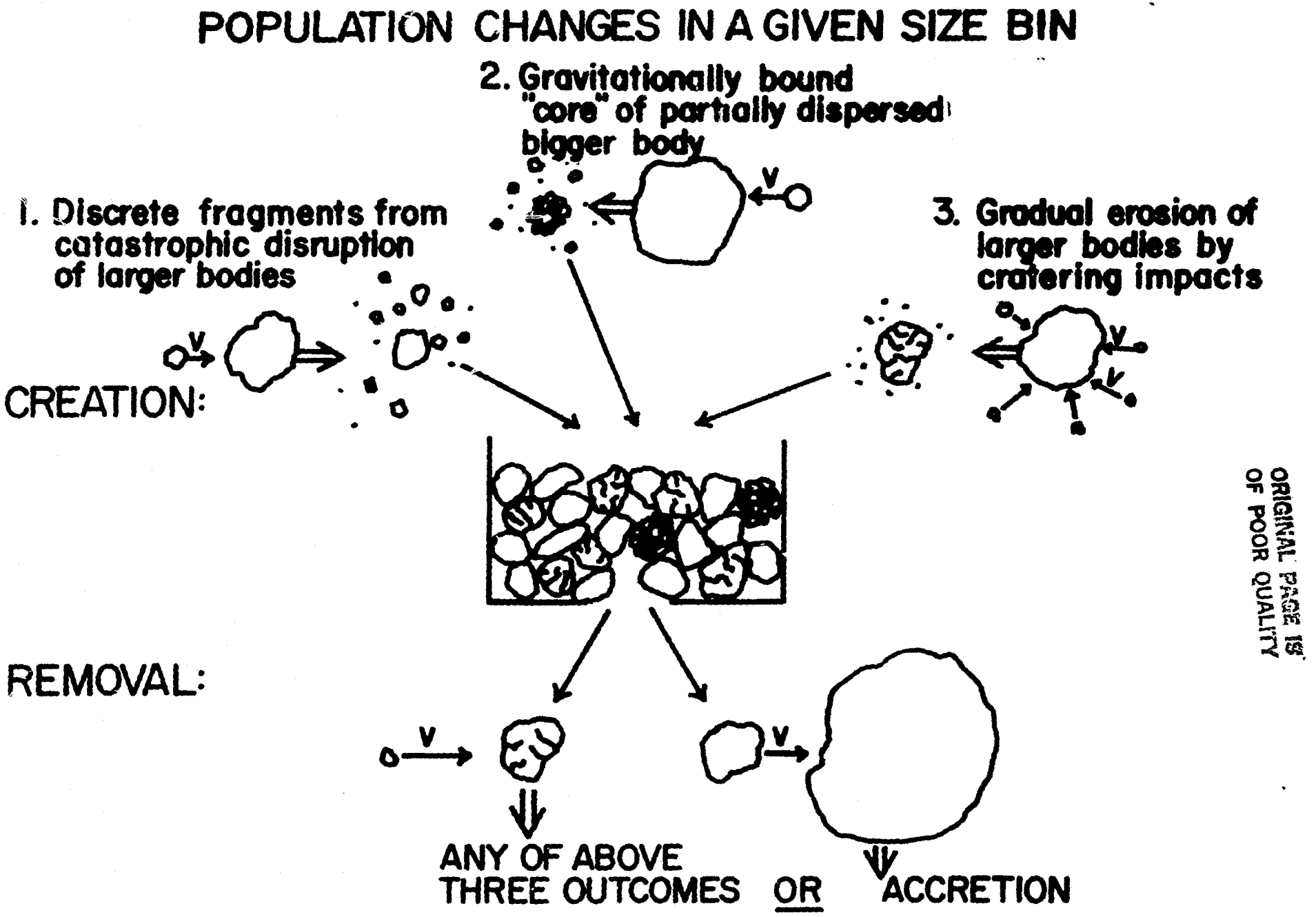

FIGURE 4: Mechanism for creation or destruction of asteroids in a diameter-size bin.

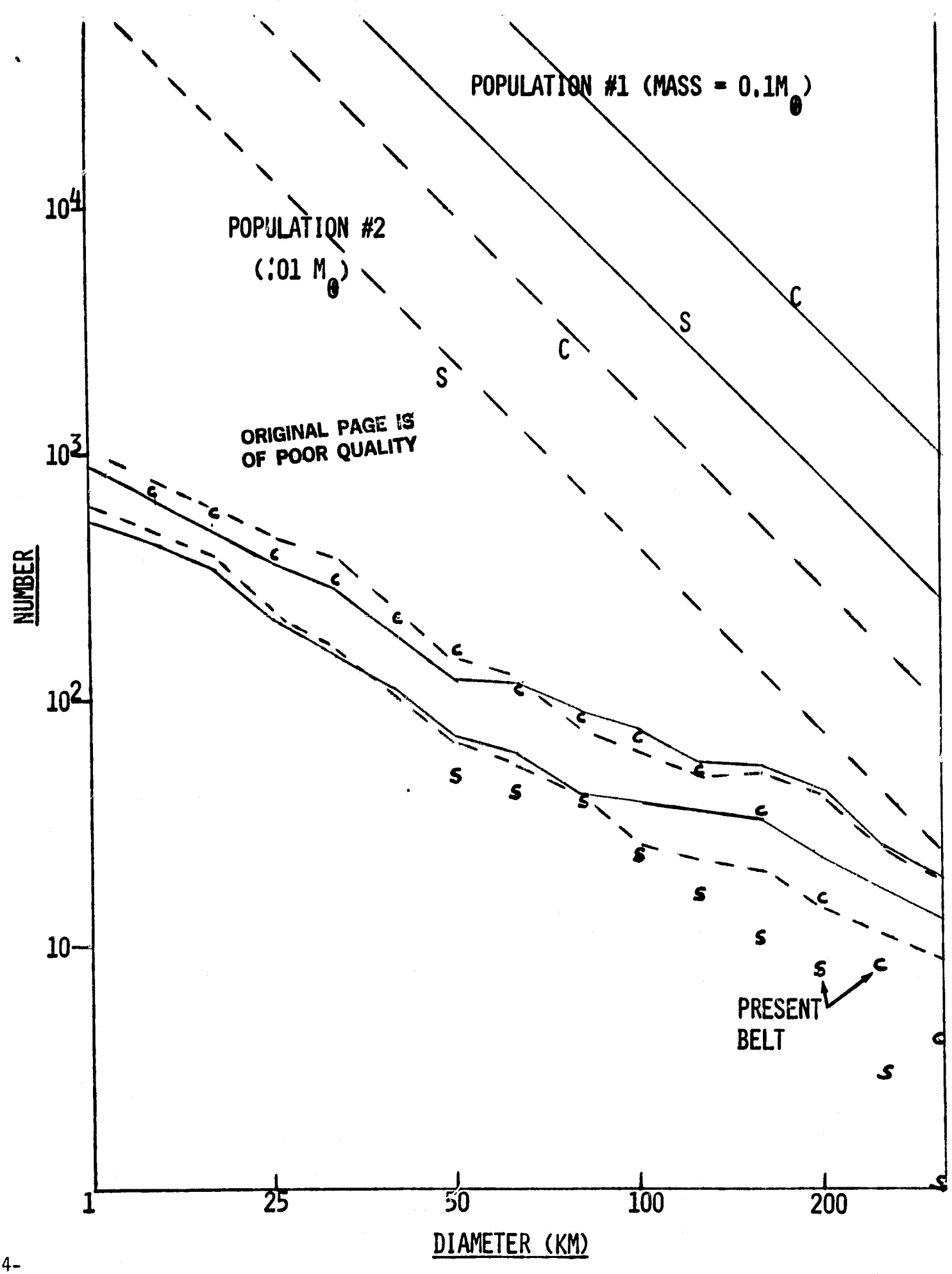

FIGURE 5: Collisional evolution of two hypothetical initial populations (solid and dashed straight lines) over the 4.5 b.y. age of the solar system.

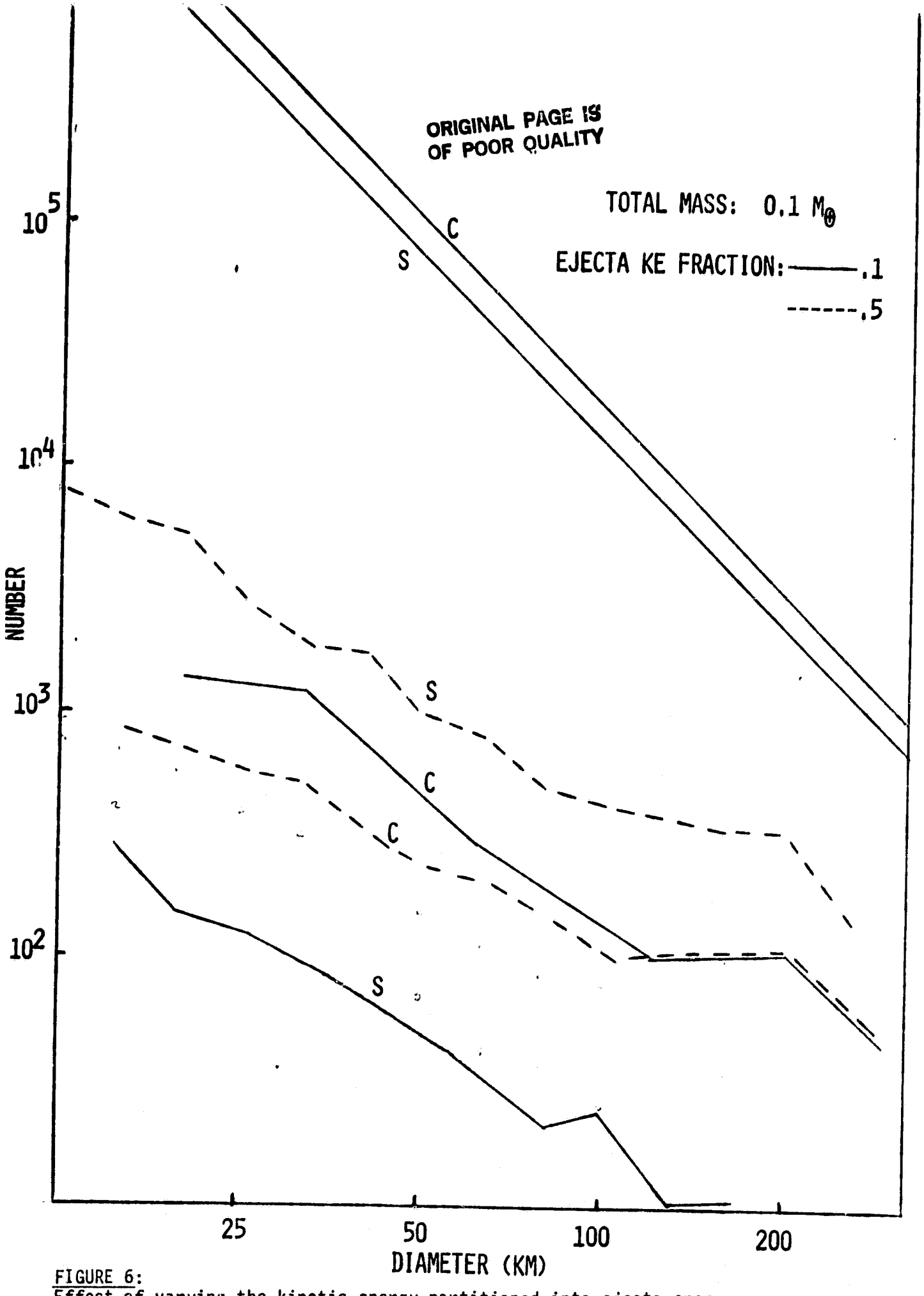

FIGURE 6:
Effect of varying the kinetic energy partitioned into ejecta energy on collision evolution.

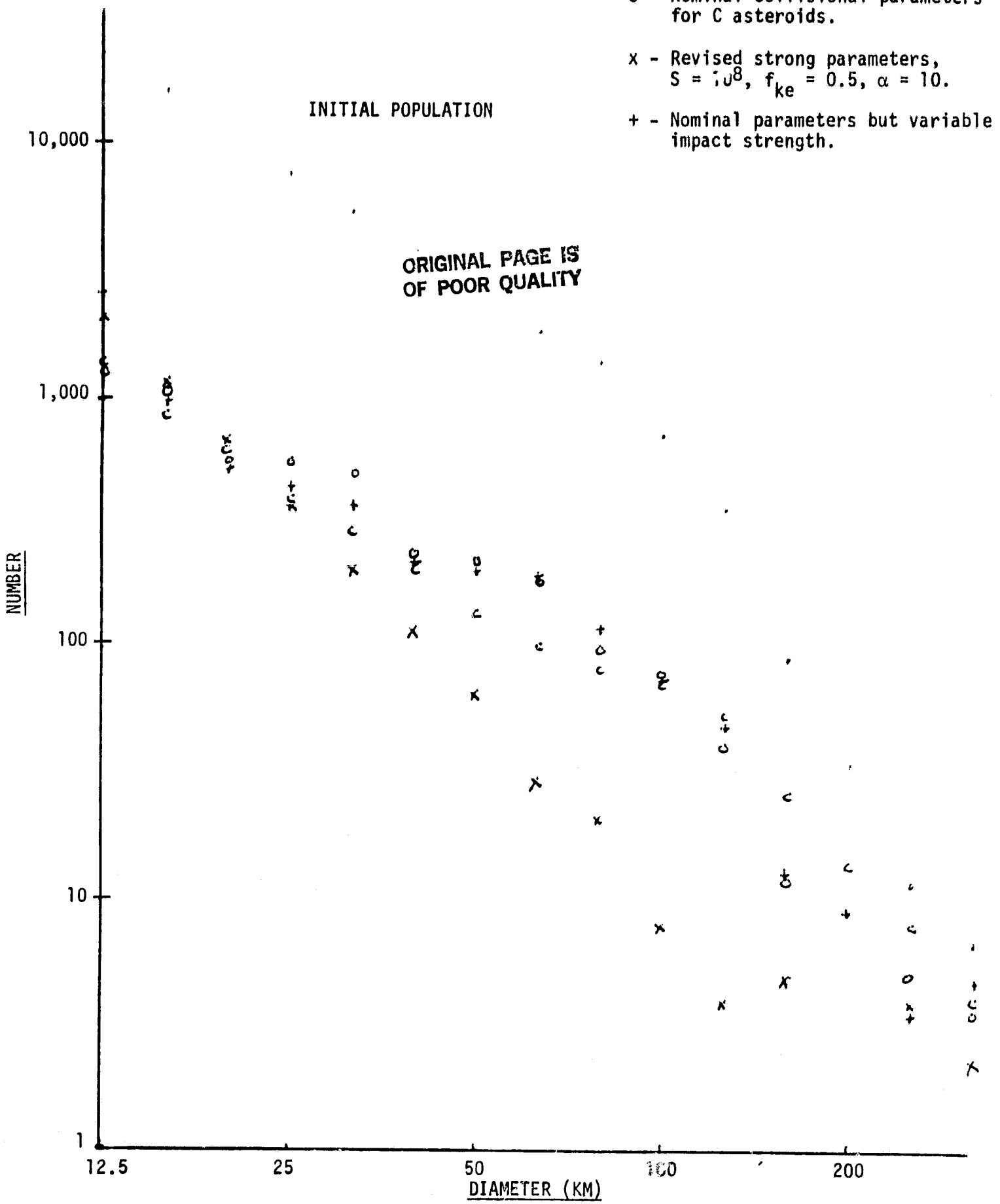

FIGURE 7: Effect of varying collisional parameters on evolution of a small mass (0.001 $M_\odot$) initial belt.

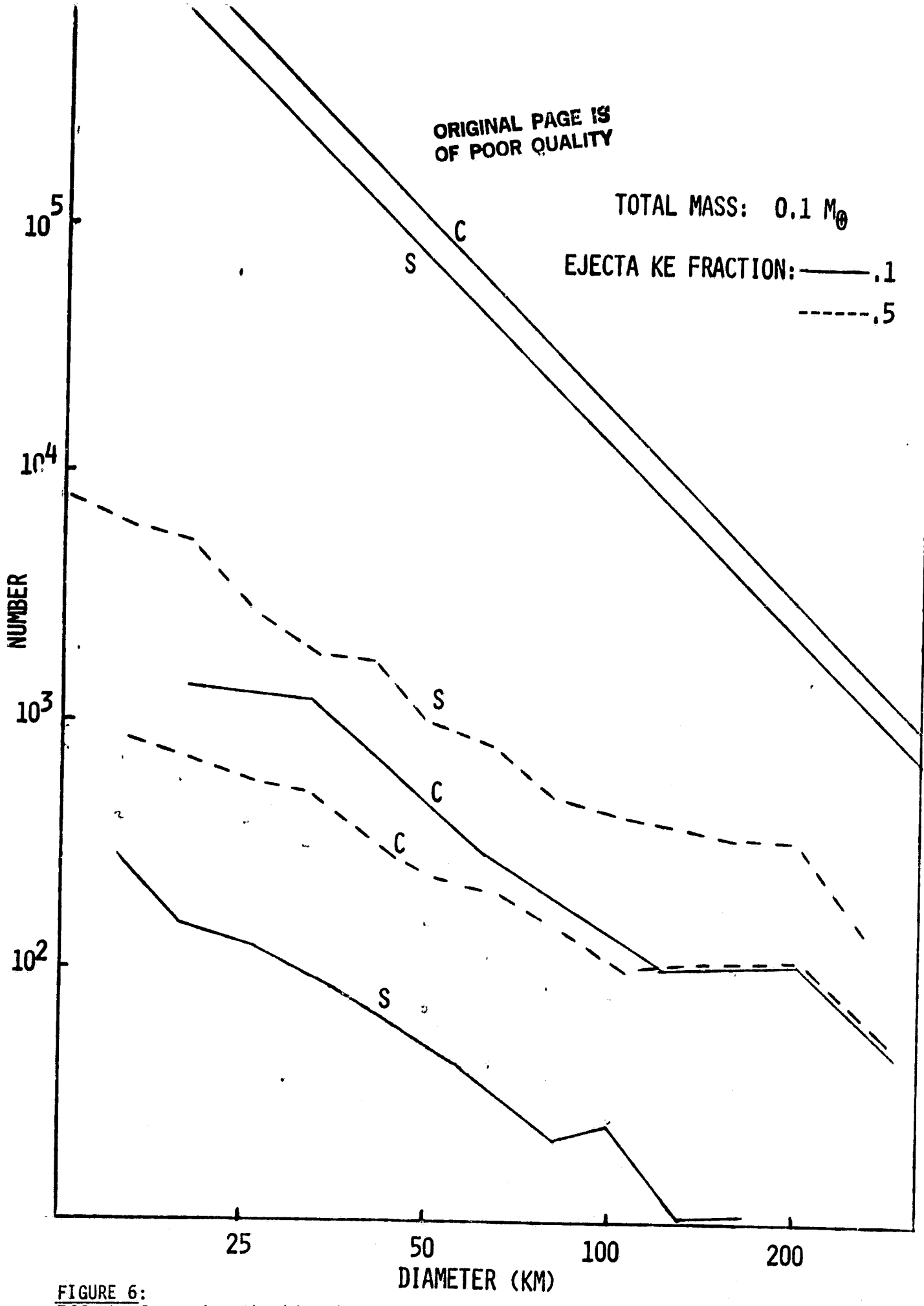

FIGURE 6:
Effect of varying the kinetic energy partitioned into ejecta energy on collision evolution.

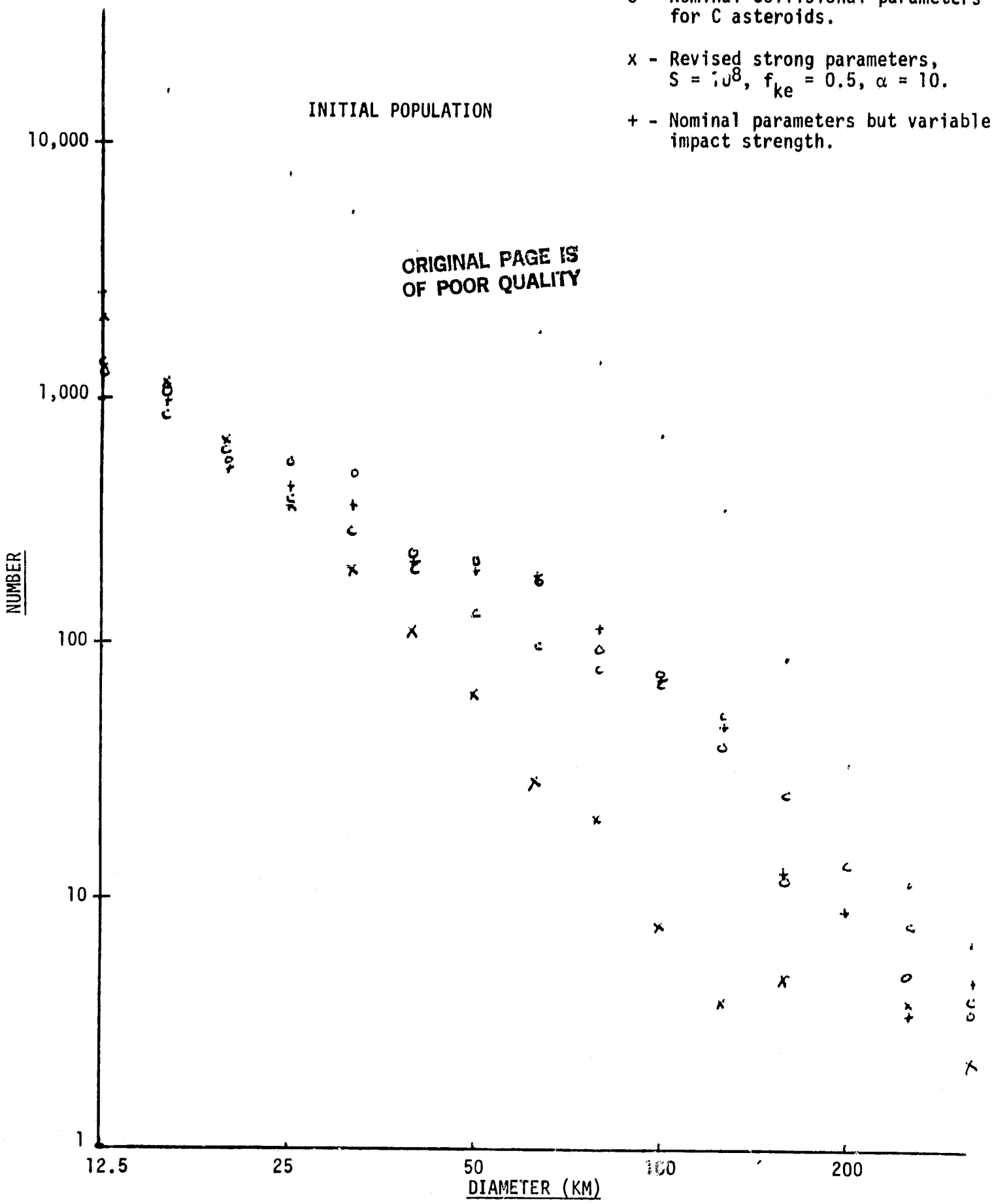

FIGURE 7: Effect of varying collisional parameters on evolution of a small mass (0.001 $M_\odot$) initial belt.

As noted, the collisionally evolved asteroid population is a mixture of collisional fragments, eroded cores, and largely intact survivors from the initial population. Figure 8 illustrates the fraction of each type of asteroid as a function of size for the small (0.001 $M_\oplus$) belt among both C and S asteroids. This result was based on the fixed impact strength model and gives the surprising result that down to sizes as small as 25 km only a small fraction (~20%) of the asteroids are fragments from collisions. Most small asteroids, although the fractions are different for C and S asteroids, are either survivors from the original population or are bodies which have been eroded down from larger sizes. The lack of 25-km fragments is due largely to the fact that there are not very many produced in our models -- catastrophic disruption of larger bodies dominantly held together by gravity produces fragments that are typically much smaller than ~25 km. Clearly, we need to re-examine this outcome in light of our new variable impact strength model. Figure 9 shows the degree to which asteroids have been shattered without being dispersed, again using the fixed impact strength model. This figure shows, as a function of size, the average collisional energy delivered to a unit mass of the asteroid by non-disruptive collisions, normalized to the impact strength of the asteroidal material. In this case, even the minimal collisional evolution produces C asteroids that have been impacted enough to deliver energies that are many multiples of their impact strength, suggesting that weak C asteroids would be thoroughly smashed throughout much of their interiors.

B. Oblique Impacts and Rotational Evolution:

In addition to changing effective energy partitioning and fragment sizes, oblique impacts impart angular momentum to a target, altering its rotation rate. Thus, the observed rotation rates of asteroids may constrain their collisional history and their physical properties, such as strength and density.

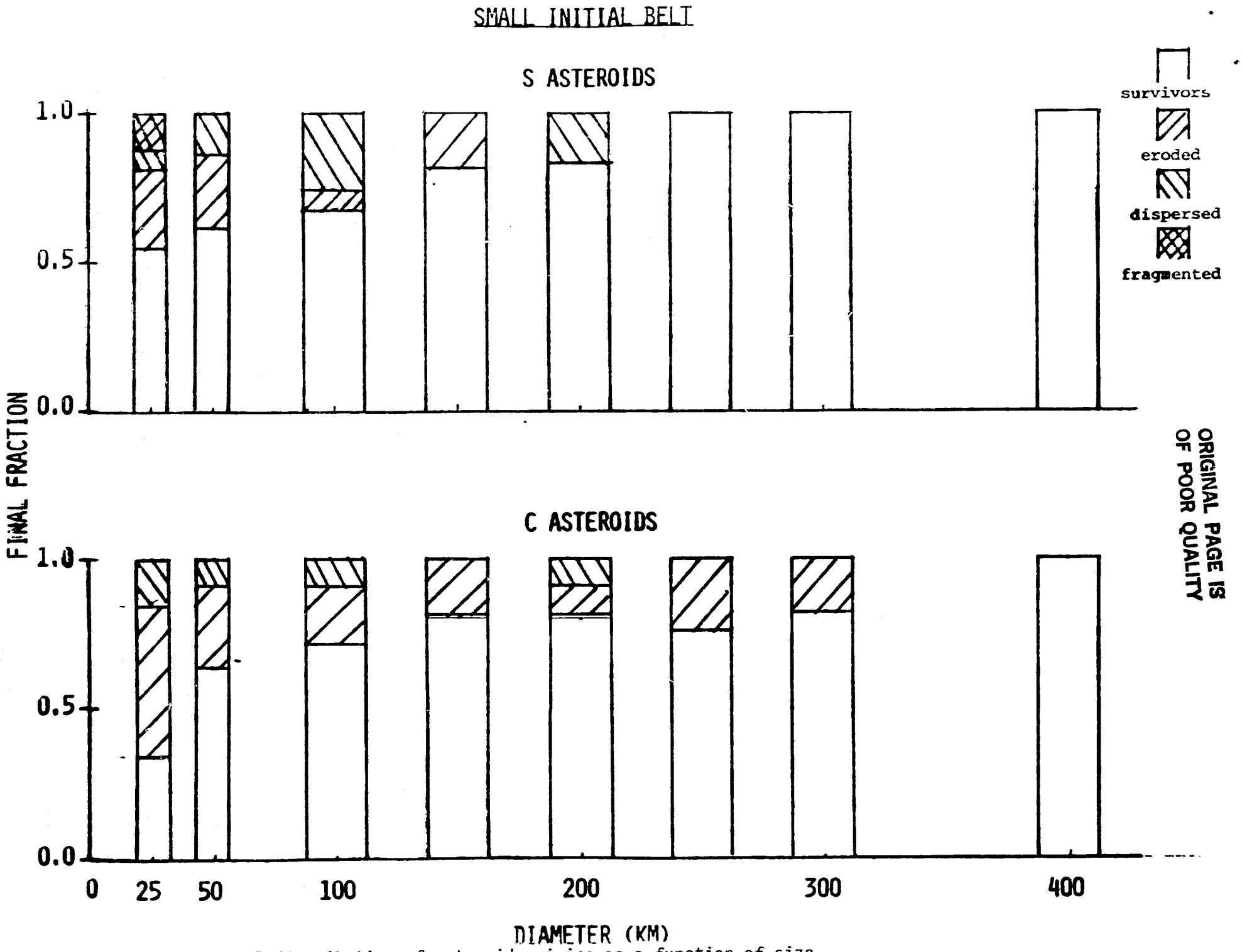

FIGURE 8: Typical distribution of asteroid origins as a function of size

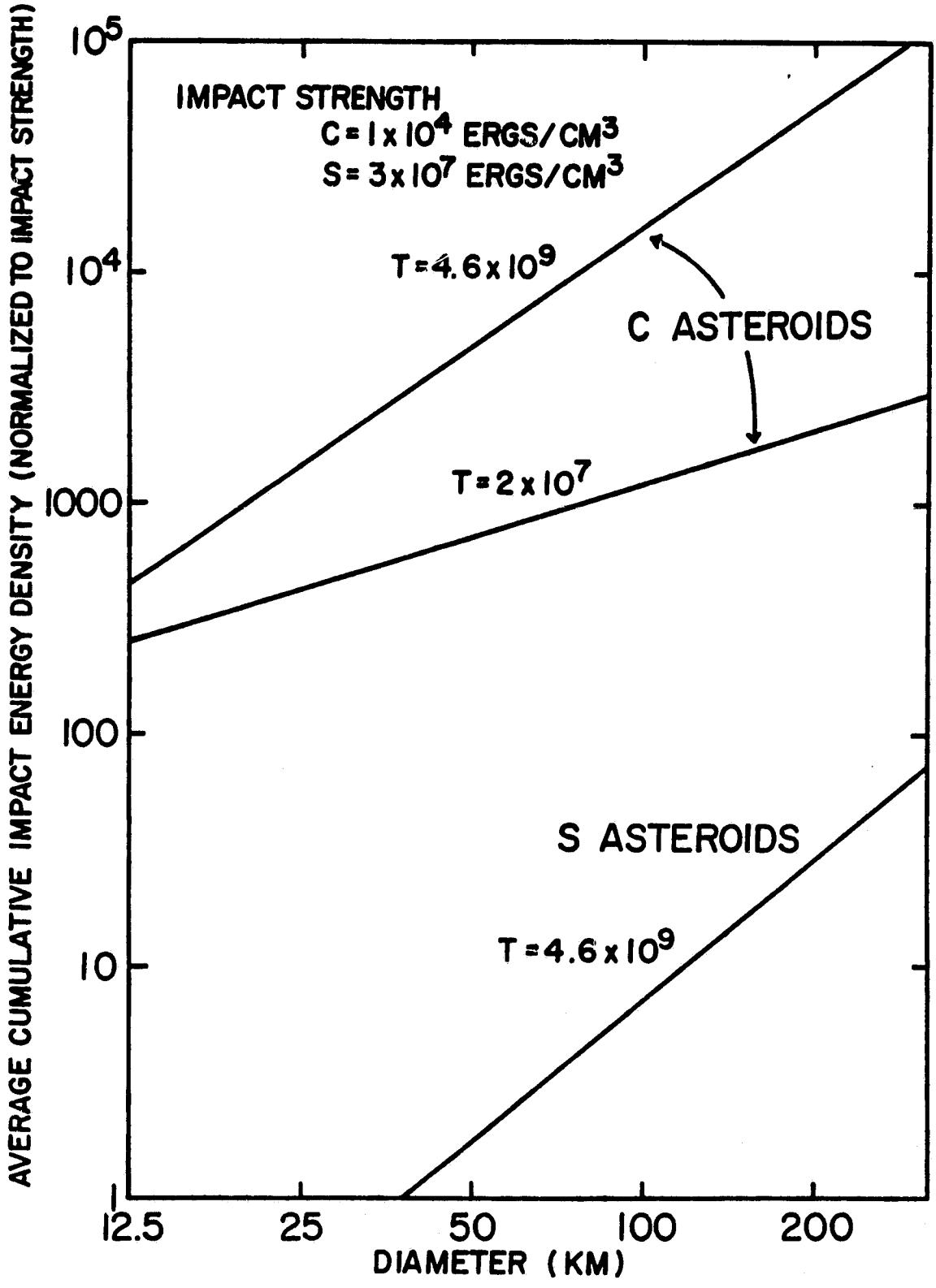

FIGURE 9: Average degree of collisional shattering for non-dispersed asteroids for a small initial mass belt.

Harris (1979) developed an analytic theory for collisional evolution of asteroid rotations. He shows that, on average, large impacts tend to increase the spin rate, and small ones to decrease it, and he derived an expression for an equilibrium rotation rate. Harris assumed that a gravitationally-bound asteroid would be disrupted by an impact involving twice its binding energy. This assumption (equivalent to $f_{ke} = 1$ in our model) led him to conclude that most asteroids would be destroyed before their spins would be altered significantly. Davis et al. (1979) point out that more plausible parameters allow more evolution of spins, but predict mean spin periods much shorter than are observed. However, Weidenschilling (1981) shows that "rubble piles" would become rotationally unstable at spin periods near the observed limit of about four hours. Collisionally induced fission of such bodies would produce binary asteroids.

A single collision may involve enough angular momentum to greatly change an asteroid's spin period. In the center of mass frame, the angular momentum is

$$H_p = \frac{m_p m_t v b}{(m_p + m_t)} \tag{15}$$

As gravitational focusing is generally unimportant for asteroids, the maximum impact parameter is roughly the target radius R. Using eqs. (4) and (15) with $\alpha = 9/4$, a gravity-dominated target would be catastrophically disrupted by an impact with $m_p/m_t \sim (10/f_{ke}) V_e^2/v^2$. If the angular momentum was shared equally by the target and escaping ejecta, an initially non-rotating asteroid could be given a spin period as short as $3.5\ f_{ke}$ hr. The actual situation is more complex, as we would expect angular momentum to be preferentially carried off by high-speed ejecta, and f_{ke} may itself be a function of impact parameter (i.e., of the angle θ). Still, we see that the effect of a single impact can be large,

in principle. In fact, the slope of the asteroidal mass distribution implies that an asteroid's spin rate is dominated by the largest impact (or the few largest) it has experienced.

In order to make his analytic theory tractable, Harris was forced to make simplifying assumptions equivalent to treating all impacts as cratering events. Actually, the dominant impacts are shattering events, in which the entire target mass is mobilized as "ejecta". In order to model these events more realistically, we have constructed a numerical simulation program that follows the stochastic evolution of a single target asteroid due to a series of impacts. Each impact is treated in the following manner: (a) The initial mass and spin period of the target are specified; (b) A projectile mass and impact velocity are chosen at random from appropriate probability distributions; (c) The impact point and direction, defined relative to the pre-impact pole of rotation, are chosen randomly; (d) The ejecta mass is computed from the impact energy and angle; (e) Kinetic energy and momentum are partitioned into the ejecta, according to algorithms which are discussed below; (f) The mass and angular momentum carried off by the escaping ejecta are calculated; (g) The remaining mass and angular momentum define the post-impact spin rate. These steps are repeated until the target is catastrophically disrupted or reaches rotational instability. While the basic concept of this program is straightforward, the algorithms for each stage can be complicated, and presumably more realistic than analytic approximations required by earlier work. Moreover, the stochastic nature of the program can determine the expected variation from the mean rotation rate for various combinations of projectile and target parameters. Our computer actually generates a repeatable series of pseudo-random numbers, so effects of varying parameters can be compared for the same set of "random" impacts.

The projectile mass m_p is chosen randomly from a power-law distribution of the form

$$dN(m) \propto m^{-q} dm \tag{16}$$

where dN is the relative number of bodies between m and m + dm. The nominal value of q is 11/6 (Dohnanyi, 1969). We must specify a lower mass bound so the program does not waste time computing an infinite number of infinitesimal impacts. The lower bound is normally set so the smallest impacts are cratering events. The formal upper bound of the distribution is $m_p/m_t = 1$, but the target is invariably destroyed by an impact with a much smaller mass ratio.

The impact velocity is chosen randomly from a gaussian distribution about a specified mean. Nominal values are $\bar{v}$ = 5 km s^{-1} with standard deviation 1.5 km s^{-1}. These values are appropriate to the main asteroid belt, and consistent with those used in our other collisional simulations. As the angular momentum is proportional to v, and the impact energy $\propto v^2$, low-velocity collisions have more potential for altering the target's spin without destroying it. However, we noticed no significant effects due to the low velocity tail of the distribution; behavior was similar to cases in which all impacts occurred at the mean velocity.

The angular momenta of the target, projectile, and ejecta are treated explicitly as vector quantities in a coordinate system defined by the target's pre-impact spin. The z-axis points in the direction of the north pole. As longitude is arbitrary, we take the x-axis to lie on the meridian of the impact, and the y-axis is defined by the right-hand rule. The impact angle, θ, is chosen from the distribution of eq. (9), equivalent to choosing the impact

parameter $b = R \sin\theta$. The impact colatitude, ϕ, is chosen so that the impact probability is uniform over the target's surface:

$$P(\phi)d\phi = 1/2 \sin\phi \, d\phi. \tag{17}$$

The azimuthal angle, ψ, measured clockwise from "north" at the impact site, completes specification of the impact direction. The components of angular momentum are:

Target:
$$H_x = H_y = 0$$
$$H_z = 0.4 m_t R^2 \Omega_o$$

Projectile:
$$H_x = -H_p \sin\psi \cos\phi$$
$$H_y = -H_p \cos\psi$$
$$H_z = H_p \sin\psi \sin\phi \tag{18}$$

where H_p is given by (15) and Ω_o is the pre-impact rotation rate.

We treat the calculation of ejecta mass somewhat differently than in our other programs. The projectile is always considered to be part of the total ejecta mass. The target contributes excavated mass, m_{ex}, proportional to the impact energy (gravity scaling for the larger asteroids has a small effect compared with other uncertainties). For competent targets, the excavated mass is proportional to $\cos^2\theta$, while for "rubble piles" it is proportional to $\cos\theta$, following results of Gault and Wedekind (1969) for cratering. The total ejecta mass is given by

$$m_{ej} = m_p + m_{ex} = m_p + C_{ex} E g(\theta), \tag{19}$$

where $g(\theta) = \cos\theta$ or $\cos^2\theta$. Note that in the limit $\theta = 90^o$ (barely grazing collision), this gives $m_{ej} = m_p$. The coefficient C_{ex} is inversely proportional

to the impact strength, S, nominally $C_{ex} = 10^{-2}\rho/S$. The target is initially assumed to be competent, with $g(\theta) = \cos^2\theta$, and S the strength of pristine material. After each impact, the size of the largest competent fragment is computed from (2) and (10); any excess mass is "regolith". Subsequent impacts assume that S is reduced (typically by a factor of 100), and $g(\theta) = \cos\theta$. If the excavated mass exceeds some fraction (nominally ½) of the regolith mass, the impact is assumed to reach pristine material, and the mass is recomputed for the competent target case. If the regolith exceeds half the total mass, the target is considered weak throughout.

The nominal collisional outcome model (Section II, above) has a discontinuity in fragment size distribution at the boundary between cratering and shattering events. The problem is more severe in accounting for angular momentum, as we must model not only the mass and velocity distributions, but the directions of the fragments. We are hampered by the lack of quantitative experimental data on oblique impacts, even for simple cratering. We have tried a number of algorithms consistent with the plausible assumptions that the degree of forward scattering (or net momentum relative to the target) and kinetic energy of the ejecta increase with θ. It should be kept in mind that the algorithms described below for momentum and energy partitioning have at best qualitative support from experimental data, and may be revised as quantitative results become available.

The energy partitioning of eq. (13) is consistent with the qualitative observation that there is little variation in crater or ejecta blanket morphology for $\theta < 45^\circ$, and the requirement that $f_{ke} \to 1$ as $\theta \to 90^\circ$. In the rotational evolution program, we make the plausible assumption that the amount of escaping high-speed ejecta increases monotonically with impact energy through the transition from cratering to shattering. We assume that shattering events yield a superposition of two ejecta components, one with the mass/velocity

distribution of cratering events, and the rest of the target mass, lacking a high-speed tail. This model is consistent with qualitative observations of shattering events by Fujiwara and Tsukamoto (1980), and unpublished data of D.R. Davis.

The mass of the "cratering" component is computed from eq. (19), with its kinetic energy given by (13). This energy is assumed to be due to a combination of motion of the ejecta's center of mass relative to the target, and radial expansion of the ejecta cloud that is azimuthally symmetric in a frame moving with the center of mass of the ejecta cloud. The ejecta cloud is assigned a net momentum (not angular momentum) tangent to the target's surface at the impact point, in the direction of the impact azimuth as defined by the angle ψ (cf. eq. 18). The fraction of the impact's momentum delivered to the ejecta, f_p, depends on both the impact angle θ and the ejecta mass:

$$f_p = \left[1 - \cos^n\theta\,(m_t - m_{ex})/(m_t + m_p)\right]^k, \qquad (20)$$

with nominal values of $n = 2$ and $k = \frac{1}{2}$. The velocity of the ejecta center of mass, and the kinetic energy associated with this motion, are determined by f_p. Subtracting this energy from the total ejecta kinetic energy (from eq. 13) gives the energy of the radial expansion of the ejecta cloud. This expansion is assumed to have the velocity distribution of eq. (4), with slope $\alpha = 9/4$.

The ejecta also carries some of the target's pre-impact angular momentum. We account for this by adding the local rotation velocity of the excavated matter to that of the ejecta. As the excavated mass need not be small compared to the target mass, the rotation velocity of the surface at the impact point is not used. Instead, the excavated mass is assumed for simplicity to be a spherical cap centered on the impact point. The rotation velocity is that of the center of mass of the cap, which lies somewhat below the surface. The ejecta

velocity is the vector sum of three motions: a "downrange" component due to the momentum of the projectile, local "eastward" velocity due to the (pre-impact) rotation of the target, and radial expansion of the ejecta cloud. The fraction of mass escaping and the angular momentum carried off are functions of azimuth; the totals are determined by numerical integration. Ejecta escapes more easily in the prograde direction. When some fraction escapes, this gives a net braking of the target's spin. This effect is absent when all or none of the ejecta escapes.

All impacts are treated by the preceding algorithm. In addition, when the impact energy is great enough to shatter the target, the velocity distribution of the remaining mass is computed as follows: The minimum ejecta velocity associated with the "crater" component is computed from eq. (5). The remaining mass (the "shattered" component) is assumed to follow a steeper power-law velocity distribution with a nominal slope of 3. The highest ejecta speed of the "shattered" material is assumed equal to the lowest velocity of the "crater" ejecta (i.e., the entire velocity distribution for the shattered body is a kinked power law with two segments of different slope. The fraction of impact energy going into kinetic energy of the shattered portion is variable, but generally several times smaller than that going into the higher-speed cratering ejecta. This algorithm is consistent with qualitative results of impact experiments by Fujiwara and Tsukamoto (1980). The shattered mass with velocity greater than escape velocity (if there is any) is assumed to carry off mean angular momentum characteristic of the surface layer of the spherical target, including the fractional part of the impact angular momentum not applied to the "crater" ejecta.

The post-impact rotational state is determined by the total non-escaping mass and angular momentum. For real asteroids, the observable quantity is not the angular momentum, but the rotation rate. This may depend on the

the internal structure -- whether the asteroid is a competent rock or a rubble pile. As mentioned above, the program keeps track of the mass of the largest competent fragment of the asteroid. If this is more than half of the total remaining mass, the asteroid is treated as a rigid, spherical body to compute the post-impact rotation rate. If less than half the mass is in the largest fragment, the rotation rate is assumed to be that of an equilibrium fluid body with its specific angular momentum (Weidenschilling, 1981). The latter always has a lower rotation rate than a rigid body with the same angular momentum. If the asteroid is a rubble pile and its angular momentum exceeds the critical value for rotational instability, binary fission is assumed. A lower limit to the period of the resulting binary is determined by assuming both components are of equal mass. Unequal components produce wider separations with longer periods. Any single case is run until a binary is produced, or the target loses more than half its mass in a single impact and is "destroyed".

Results from this rotational evolution program must be interpreted with caution. Many of its steps involve plausible but somewhat arbitrary assumptions about ejecta behavior in large collisions. Still, it is an improvement on analytic models that assume all impacts, regardless of size, are formally identical to small cratering events. We regard this program as still in development, to be improved as quantitative experimental data on catastrophic impacts become available. With these caveats, we present some results of these simulations.

We find that asteroid size has a significant effect on rotational evolution. For convenience, we define an asteroid as "large" if its gravitational binding energy exceeds its impact strength. The critical radius for this transition is proportional to the square root of the impact strength. For a density of 2.5 g cm^{-3} and strength $S = 3 \times 10^7$ $ergs/cm^{-3}$, characteristic of strong rock, the transition is at $R \simeq 50$ km. The rotational evolution model agrees

with our other collisional model in that large asteroids are generally reduced to rubble piles well before they are catastrophically disrupted. Going toward smaller sizes, a decreasing fraction of asteroids become rubble piles before disruption, but we have observed some such cases at radii as small as a few km.

Figure 10 shows results of two simulations for different asteroid strengths. In each simulation, targets had initial radii of 300, 100, 30, 10, and 3 km, and initial spin period of 10 hr. For each initial size, ten cases were run with different random inputs. Each target was followed until it was either catastrophically disrupted (i.e., lost more than half its remaining mass by a single impact) or became rotationally unstable. Spin rate is plotted vs. target radius (note that the spin period increases downward). Major impacts cause jumps in both size and rotation rate.

In Fig. 10 (a) the strength is assumed to be 3×10^7 ergs/cm^{-3} for pristine material, and 3×10^5 ergs/cm^{-3} for "rubble". The 300-km bodies retain most ejecta from small to moderate impacts. They are generally spun up to short periods before disruption by a major impact. At R = 100 km, the mean period is significantly longer. We interpret this as due to the fact that our choice of parameters allows significantly more ejecta to escape, carrying off a larger amount of angular momentum. The apparent limit of about 4 hr for the shortest periods of these large asteroids is imposed by rotational deformation and fission of rubble piles. Below R = 30 km, material strength is important. Occasionally a competent body or fragment is spun up to shorter period than could be sustained by a rubble pile. The mean spin rate appears to increase below about 10 km, but there are significant numbers of very slow rotators as well. This appears due to the small competent bodies being strong enough that a fortuitous large impact can "stop one in its tracks" without destroying it.

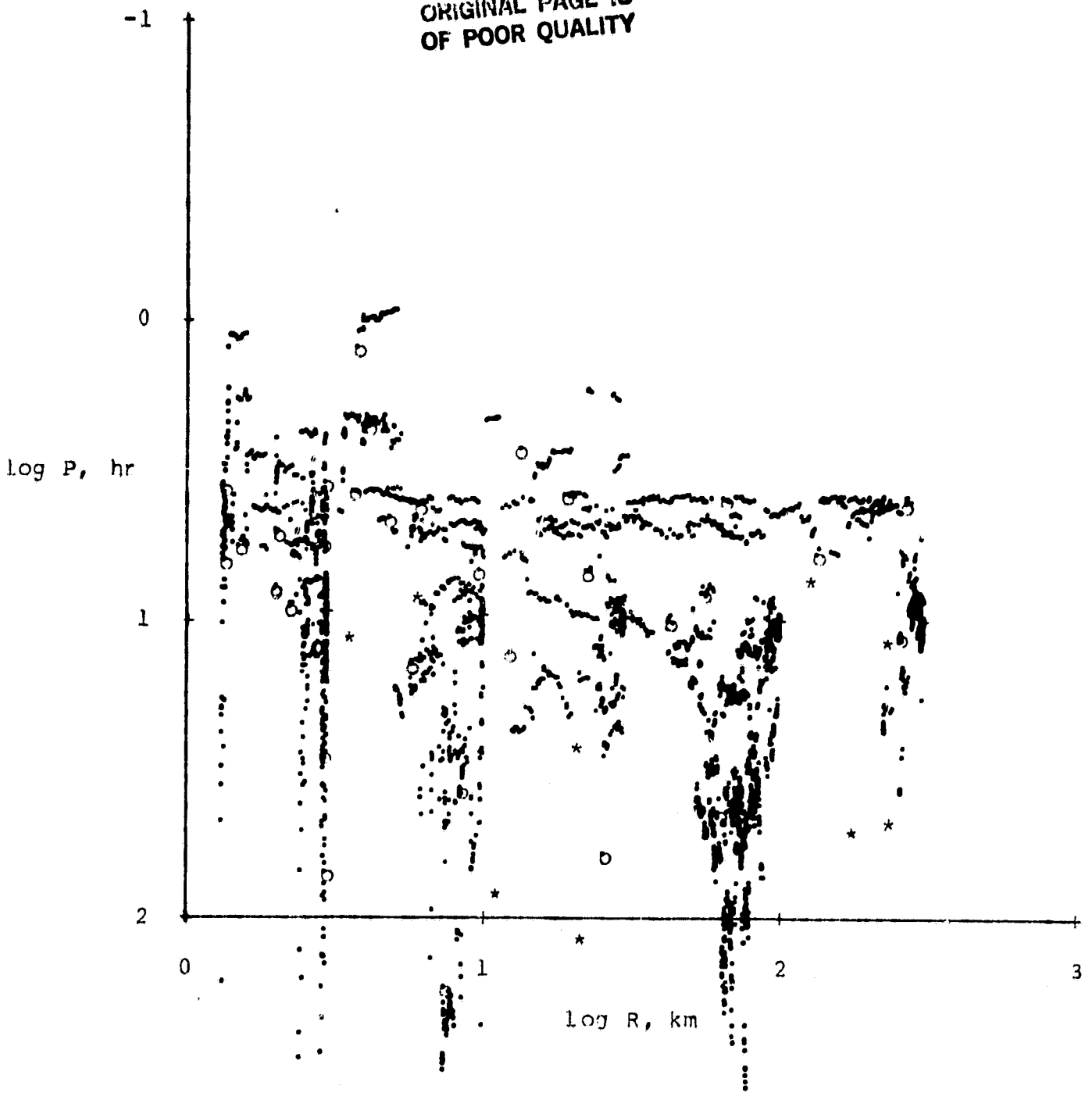

FIGURE 10 (a): Outcome of a simulation of rotational evolution. Rotation period (increasing downward) is plotted vs. target radius. Initial radii were 300, 100, 30, 10, and 3 km; initial period in each case was 10h. Ten runs were started at each initial size with a different sequence of random numbers, and followed until disruption or binary fission. Asteroids are binaries, assuming components of equal mass in synchronous rotation (unequal components would plot lower for the same angular momentum). Circles are formally computed final states of remaining mass after catastrophic disruption. This case is for impact strengths of 3×10^7 ergs/cm^3 for pristine material, and 3×10^5 ergs/cm^3 for shattered "rubble".

Figure 10 (b) shows a similar plot for weaker targets, with strengths of 3×10^6 and 3×10^4 ergs/cm^{-3} for pristine and shattered material, respectively. Material strength has little effect for the largest targets, which are dominated by gravitational binding. For somewhat smaller sizes, below $R \simeq 100$ km, there is much less variation from the mean spin period than for stronger targets, down to radii of a few km, where material strength becomes significant. Weak asteroids in this size range lose mass rapidly, and are destroyed before their angular momenta are greatly changed. For comparison, known spin periods are plotted vs. size for main-belt asteroids in Figure 11. Data are generally lacking for sizes $\lesssim$10 km, and there is observational bias against measurement of long periods. The observed range of spin periods is generally consistent with impact strengths intermediate between the two simulations shown here.

In our simulations, a significant fraction (~20%) of large asteroids undergo binary fission before catastrophic disruption. There are observational data suggesting that some asteroids are binary (Binzel and Van Flandern, 1979), although none has been shown conclusively to be so. Our collisional model, consistent with present knowledge of impact behavior, supports the existence of binary asteroids as natural products of collisional evolution of the asteroid belt. In our simulations, binaries result from prograde impacts on targets which are already shattered and spinning rather rapidly ($P \lesssim 6$ h) due to previous impacts.

The phenomena associated with shattering impacts on finite targets are complex and poorly understood, compared with simple cratering. Our future work will continue testing of plausible algorithms for momentum and energy partitioning to test the sensitivity of our results to these assumptions. The parameter space to be explored is large, but this effort should allow

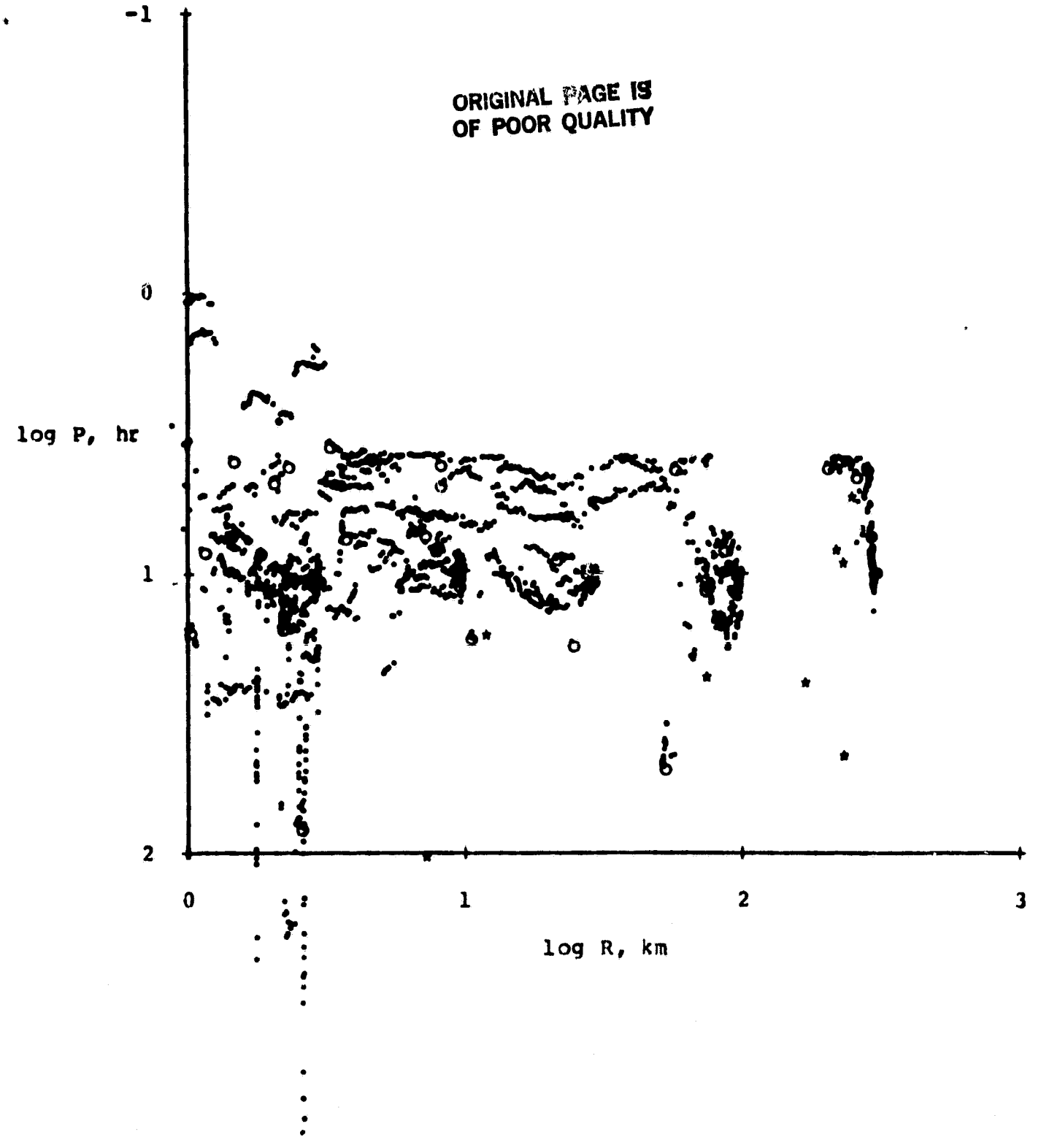

FIGURE 10 (b): As in (a), but with strengths of 3×10^6 and 3×10^4 ergs/cm^3 for pristine and shattered material, respectively. The apparent limit at $P \simeq 4h$ is imposed by rotational deformation and fission of "rubble piles".

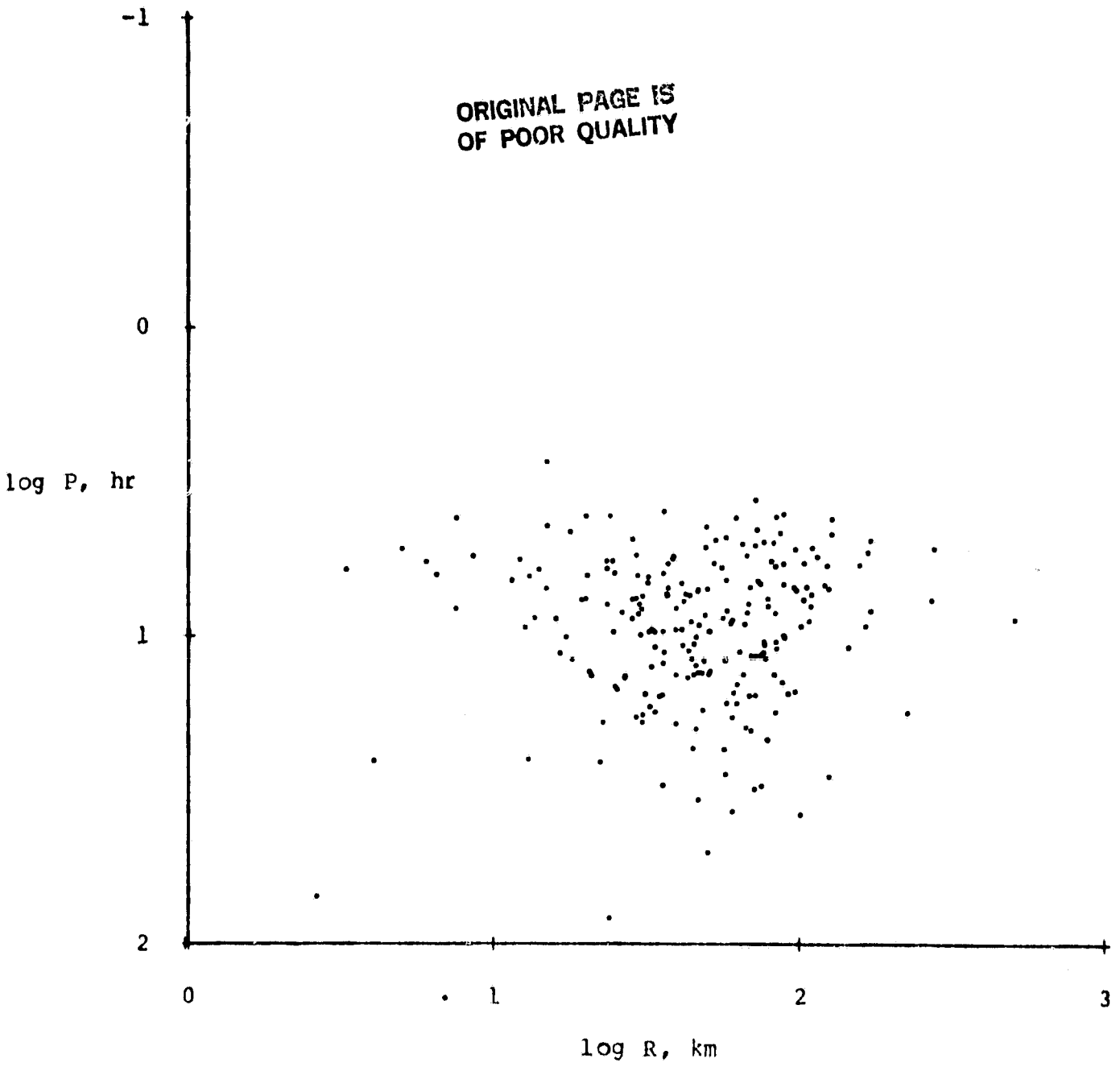

FIGURE 11: The observed distribution of spin periods and radii for main-belt asteroids. Surveys are biased against small objects and slow rotators, but the two points at $P > 10^2$h and $P > 10^3$h are real.

the observed distribution of asteroid rotation rates to constrain geological properties, such as density and impact strength.

V. Future Directions

We will continue our studies of asteroid collisional evolution in two major areas: (i) application of the collisional size evolution model to explore asteroid collisional evolution, the present physical state of asteroids and their relation to meteorites, and (ii) synthesis of the separate size and spin collisional models into a single program that models the simultaneous evolution of asteroid sizes and rotation rates.

We must address further the problem of scaling of asteroid impact strengths. We will explore further the model proposed above by examining fracture dynamics theory and by drawing upon results from explosive shots in terrestrial application (e.g., construction, moving, oil shale extraction, etc.). We will also test the collisional outcome model against all available Hirayama family data; a necessary condition for any collisional outcome algorithm is that it must reproduce the observed Hirayama families for plausible impact parameters. Further collisional evolution studies will commence only after the collisional model has been finalized.

Integration of both the size and spin program into a single model will provide a valuable tool for understanding the collisional evolution for arbitrary populations. Sizes and spins together will provide more constraints that the final population must satisfy, and this should enable us to better understand the early history, evolution, and physical state of asteroids.

REFERENCES

1. Chapman, C.R. and D.R. Davis (1975), Science 190, 553-556.

2. Davis, D.R., C.R. Chapman, R. Greenberg, and S.J. Weidenschilling (1982), (Abstract), BAAS 14, 720.

3. Davis, D.R., C.R. Chapman, R. Greenberg, S.J. Weidenschilling, and A.W. Harris (1979), in Asteroids, T. Gehrels, ed., 528-557.

4. Dohnanyi, J.S. (1969), JGR 74, 2531.

5. Dohnanyi, J.S. (1971), in Physical Studies of Minor Planets, T. Gehrels, ed., NASA Sp-267, 263.

6. Fujiwara, A (1982), submitted to Icarus.

7. Fujiwara, A., G. Kamimoto, and A. Tsukamoto (1977), Icarus 31, 277-288.

8. Fujiwara, A. and A. Tsukamoto (1980), Icarus 44, 142-153.

9. Gault, D.E., E.M. Shoemaker, and H.J. Moore (1963), NASA Tech. Note D-1767.

10. Gault, D.E. and J.A. Wedekind (1969), J. Geophys. Res. 74, 6780.

11. Gradie, J.C. (1978), Ph.D. Dissertation, University of Arizona.

12. Gradie, J.C., C.R. Chapman, and J.G. Williams (1979), in Asteroids, T. Gehrels, ed., 359-390.

13. Greenberg, R.G., J.F. Wacker, W.K. Hartmann, and C.R. Chapman (1978), Icarus 35, 1-26.

14. Harris, A.W. (1979), Icarus 40, 145-153.

15. Hartmann, W.K. (1980), 11 LPSC Abstracts, 404.

16. Hartmann, W.K. (1978), Icarus 33, 50-61.

17. Stöffler, D., D.E. Gault, J. Wedekind, and G. Polkowski (1975), J. Geophys. Res. 80, 4042.

18. Weidenschilling, S.J. (1981), Icarus 46, 124-126.